

---

# **Topographic Maps**

---

**Nicholas M. Gale**

*Supervisor:* Professor Stephen Eglen

*Supervisor:* Professor Kristian Franze

Doctoral Thesis submitted as part of the PhD degree in the  
Department of Applied Mathematics and Theoretical Physics  
University of Cambridge

Date of submission: xx/xx/22

---

---

This is to certify that this work meets the requirements and standard expected for the degree Doctor of Philosophy (PhD) at the University of Cambridge. The work is my own and does not breach any ethical rules with regard to the conduct of the research.

**Student:** Nicholas Gale

---

*Signature*

---

*Date*

# Acknowledgements

## Abstract

Topographic maps are ubiquitous brain structures that are fundamental to sensory and higher order systems and are composed of connections between two regions obeying the relationship: physically neighbouring cells in a pre-synaptic region connect to physically neighbouring cells in the post-synaptic region. The developmental principles driving topographic map formation are usually studied within the context of genetic perturbations coupled to high resolution measurements and for these the mouse retinotopic map from retina to superior colliculus has emerged as a useful experimental context. Modelling coupled with genetic perturbation experiments has revealed three key developmental mechanisms: neural activity, chemotaxis, and competition. Some principal challenges in modelling this development include explaining the role of the spatio-temporal structure of patterned neural activity, determining the relative interaction between developmental components, and developing models that are sufficiently computationally efficient that statistical methodologies can be applied to them.

Neural activity is a well measured component of retinotopic development and several independent measurement techniques have recorded the existence of spatiotemporally patterned waves at key critical points during development. Existing modelling methodologies reduce this rich spatiotemporal context into a distance dependent correlation function and have subsequently had challenges making quantitative predictions about the effect of manipulating these activity patterns. We use a neural field theory approach to develop mathematical theory which can incorporate these spatiotemporal structures. We then perform Bayesian MCMC regression analysis on biological measurements to assess the accuracy of the model and make predictions about the time-scale on which activity operates. This time scale is tuned to the length of an average wave pattern suggesting the system is integrating all information in these waves.

The interaction between chemotaxis and neural activity has historically been thought of as linearly independent. A recent study which perturbs both developmental mechanisms simultaneously has suggested that these two are highly stochastic and regular development depends on a critical fine-tuned balance between the two: the heterozygous phenotype was observed to present as both a wild-type and homozygote for different specimens. We test this hypothesis against the data-set used to generate it. By recreating the entire experimental pipeline *in silico* with the most parsimonious existing model we are able to account for the data without the need to appeal to stochasticity in the mechanisms. A statistical analysis demonstrates that the heterozygous state does not significantly overlap with the heterozygotes and that the stochasticity is likely due to the

---

---

measurement technique.

The existing models are computationally demanding; at least  $O(n^4)$  in the number of retinal cells instantiated by the model. This computational demand renders these classes of models incapable of performing statistical regression and means that their parameters spaces are largely unexplored. We develop a modelling framework which integrates the core operating mechanisms of the model but when implemented on modern GPU computational architectures is able to achieve a sub-linear complexity. We then demonstrate that this model captures the explanatory power of existing modelling methodologies.

We finally explore the role of competition in a dimensional reduction framework: the Elastic Net. The Elastic Net has been used both as a heuristic optimiser (validated on the NP-complete Travelling Salesman Problem) and to explain the development of cortical feature maps. We demonstrate that the addition of competition acts as a counter-measure to the feature distorting components of the Elastic Net as a cortical map generator. We further demonstrate that competition substantially improves heuristic performance on the Travelling Salesman Problem making it competitive solvers when solution times are normalised. The heuristic converges on a length scaling law that is discussed in the context of wire-minimisation problem.

# Contents

<b>1</b>	<b>Opening Remarks</b>	<b>1</b>
<b>2</b>	<b>Lattice Method Analysis: Analysing a Stochastic Development Hypothesis</b>	<b>2</b>
2.1	Preface . . . . .	2
2.2	Introduction . . . . .	2
2.3	Data Analysis . . . . .	4
2.4	Modelling Pipeline . . . . .	9
2.4.1	Anatomical Model . . . . .	10
2.4.2	Activity Spiking Model . . . . .	11
2.4.3	Optical Image Scan Reconstruction . . . . .	12
2.5	Results . . . . .	12
2.5.1	Anatomical Experiments . . . . .	12
2.5.2	Lattice Analysis . . . . .	13
2.5.3	Statistical Discrimination of Phenotypes . . . . .	18
2.5.4	Activity Perturbations . . . . .	19
2.6	Discussion . . . . .	20
<b>3</b>	<b>Concluding Remarks and Future Work</b>	<b>26</b>
	<b>References</b>	<b>33</b>

# List of Figures



- 2.6 We present the azimuthal phase diagrams for several heterozygote simulations and a homozygote simulation. Panel (a) corresponds to  $\Delta R = 0.8$  and resembles a HETA type classification. Panel (b) corresponds to  $\Delta R = 1.0$  and resembles a HETB type classification. Panel (c) corresponds to  $\Delta R = 1.2$  and resembles a HETC type classification. Panel (d) corresponds to  $\Delta R = 2.0$  and resembles a HOM classification. This demonstrates that under choices which correspond to experimentally observed knock-in values the optical imaging procedure can recreate the properties of the functional imaging data in biological specimens [59, 51]. . . . . 15
- 2.7 A series of whole maps and part-maps generated on anatomical data for a heterozygote type simulation. The blue represents a projection from the field into the colliculus and the part maps are generated by conditioning the pre-image on Islet2-EphA3 and wild-type cells respectively. The black represents a projection from the colliculus to the field and the part maps are derived by segregating the colliculus into rostral and caudal regions using the average location of the filtered points as a discriminant. The remove links in the whole map can be seen in red and the projection overlap is highlighted in purple. . . . . 16
- 2.8 Two series of part-map lattices are shown with increasing  $\Delta R$  in steps of 0.4 from left to right. The field-to-colliculus are presented on the top row and several notable features are discussed. First, the distinction between the EphA3 and wild-type projections is apparent in the relative densities of the lattice map that the algorithm generates. Second, the wild-type projection predominately inhabits the caudal region but can be seen to overlap into the far rostral region until very high levels of  $\Delta R$ . The colliculus-to-field maps are shown in the bottom row. The noise introduced by the optical imaging procedure in the region of intermingling maps increases with  $\Delta R$  mimicking what we observe biologically. Both the rostral and caudal regions from a progressively larger cover of the visual field but the rostral region is of slightly lower quality. This is likely due to the compression of the EphA3 projection into the rostral region of the colliculus. . . . . 17
- 2.9 The VFO distributions are shown as a function of increasing EphA3. There is a notable critical value at approximately  $\Delta R = 0.2$  to  $\Delta R = 0.4$  where the VFO becomes no-zero. It then smoothly increases up to a value of 0.8 at the homozygous level of  $\Delta R = 2.0$ . The distributions imply that at the experimentally measured levels of EphA3 knock-in for homozygotes and heterozygotes it is not likely that they can come from the same distribution. . . . . 19

---

2.10 The distribution for the mean projection location of each cell type as an increasing function of $\Delta R$ . The projections can be seen to immediately separate and become significantly different at $\Delta R = 0.6$ . This validates the VFO as a measurement to discriminate the existence of two projections. . . . .	20
2.11 The distributions for the whole and individual part maps are shown in blue, red, and yellow respectively. The whole map quality begins to deteriorate at $\Delta R = 0.4$ and is significantly different from the part maps at $\Delta R = 0.8$ . The whole map quality continues to decrease with increasing $\Delta R$ while the part maps remain relatively high quality for $\Delta R > 0.8$ . The part-map quality returning to 90% is quantitatively in line with the measured values for wild-type maps and part-maps biologically. This supports the existence of two distinct projections for $\Delta R > 0.8$ which corresponds well to the experimentally measured values for the additional knock-in EphA3 [34].	21
2.12 A series of injection experiments are performed on knock-in simulations with $\Delta R$ increasing left to right from $\Delta R = 0$ (wild-type) to $\Delta R = 2.0$ (HOM). The result of increasing the strength of activity relationships by setting $\gamma = 0.0625$ is shown in panel (a) and demonstrates a complete map collapse to the wild-type phenotype. Panel (b) shows that when the activity is downregulated to $\gamma = 0.000625$ there are reversals in polarity for high $\Delta R$ and map collapse for low $\Delta R$ . The effect of mimicking the $\beta 2$ correlation profile is shown in panel (c) and shows the map phenotypes are maintained but receptive fields are widened. . . . .	22

# Chapter 1

## Opening Remarks

## Chapter 2

# Lattice Method Analysis: Analysing a Stochastic Development Hypothesis

### 2.1 Preface

The following chapter contains work from the paper **Detailed analysis of the double functional maps in EphA3 knock-in mice** researched and written in collaboration with David Willshaw at the University of Edinburgh. The research aim was to rigorously investigate the claim that the EphA3 heterozygote is on the border of a bifurcation point where it can phenotypically present itself in a stochastic manner as a wild-type, homozygote, or some mixed state in between, dependent on the activity [51]. The data analysis using the lattice method was performed by primarily by David Willshaw and will be included in this chapter to contextualise the theoretical results. The predominate focus of the chapter will be to recreate the experimental pipeline computationally and use modelling efforts to interrogate the central claim of stochasticity in the development of heterozygous mice.

### 2.2 Introduction

The individual effects that chemotaxis and neural activity have been discussed in both experimental and modelling contexts and subsequent theory has been developed for the individual contribution of these mechanisms: chemotaxis establishes a coarse topography on the basis of relative signalling

while neural activity works to refine this interaction through a spatio-temporal patterning of spontaneous activity before eye-opening; see section ?? for a complete review and Chapter ?? for a detailed account of modelling activity in the wild-type and  $\beta 2^{-/-}$  genotype cases. The relative effects that these two developmental systems have on each other is less clearly understood with suggestions that activity patterns may regulate Eph/ephrin expression [45, 50]. A recent hypothesis is that chemotaxis and activity are finely balanced in the wild-type mouse but stochastic map generation can be achieved by manipulating chemical gradients and thus these mechanisms are ultimately stochastic in nature [51].

This hypothesis was developed by performing intrinsic optical imaging scans on the superior colliculus of several wild-type and mouse mutants: EphA3 $^{+/-}$ , and EphA3 $^{+/+}$  knock-ins and combined EphA3 $+\beta 2^{-/-}$ . As discussed in Section ?? the EphA3 receptor is not endogenous to mouse and it is knocked in on the Islet2 expressing cells in the retina resulting in a boost of EphA receptor in a random salt-and-pepper distribution across the retina [13, 59]. Retrograde DiI injections revealed that in the homozygous knock-in a complete duplicated map is formed: for every retinal injection site there are two termination sites in the superior colliculus along the rostrocaudal axis. The heterozygotes follow a similar relationship but the duplicated projections are restricted to the caudal region of the colliculus collapsing into a single projection rostrally [12]. These make it an excellent candidate to study perturbative effects in chemical signalling.

An intrinsic optical imaging scan is performed by stimulating a mouses visual field with a regular periodic signal and measuring the phase of the induced activity in the colliculus: the phase should correlate with the average retinal position of the signal along the stimulating axis; see Section ???. Optical imaging scans revealed that the homozygous knock-ins reliably produced a functional double map suggesting that the wild-type and EphA3 $^{+/+}$  populations are segregated [16]. The technique was then performed on heterozygous knock-ins by Owens et. al. (2015) and revealed a highly variable phenotype: it would phenotypically present as a wild-type, a homozygote, and a class of mixed state in between; see Figure 2.1. To understand this variability in the context of activity they disrupted activity patterns by creating a EphA3 $+\beta 2^{-/-}$  mutant and remarkably optical imaging experiments revealed that the variable heterozygous states collapsed into a wild-type phenotype. These results were corroborated with a computational model which can phenomenologically reproduce the EphA3 $^{+/+}$  phenotype by adding additional EphA  $\Delta R$  in a salt-and-pepper fashion to its gradients. They demonstrated that when this  $\Delta R$  was tuned to a point in-between wild-type and homozygous levels the model qualitatively produced maps similar to those observed experimentally. These data were collectively interpreted in the following fashion: there exists a fine balance between activity and chemotactic developmental mechanisms. The heterozygous knock-in exists on the border of a bifurcation point between the regular wild-type and homozygous mapping.

At this bifurcation point the model suggests activity dependent mechanisms stochastically cause the heterozygote present in a heterogenous plethora of states.

These data and observations provide several interesting challenges from a theoretical perspective with the principle question being: where is the stochasticity in the data arising from? The model is stochastic but this does not necessarily imply stochasticity in the developmental mechanisms but is used rather as a minimisation technique [72]. Critically, the model enforces a one-to-one mapping between retinal and collicular locations which implicitly models the competitive nature of development but is arbitrarily strict and physically unrealistic. When combined with the Metropolis-Hastings methodology for energy minimisation this condition limits the search space of possible maps and can introduce artefacts not related to the underlying biology. The model was updated to include a more realistic realisation of competition and is a more appropriate theoretical tool to investigate this hypothesis with [69]. The stochastic nature of the data also provides an avenue to explore the underlying statistical properties of the model and methodologies to explore its parameter space which has not been historically done; see Section ???. We will proceed first by summarising the data analysis performed by Owens et. al. (2015) and providing additional analysis which will contextualise the modelling work [51]. We will then develop a pipeline which is able to capture the intrinsic optical imaging process so that we can unite the functional maps recorded with the underlying anatomy predicted by the model. This pipeline will allow to generate lattice objects which we can compare with the biological data and generate distributions of relevant statistics to explore the principal hypothesis.

## 2.3 Data Analysis

The dataset is comprised of intrinsic optical imaging scans from 16 EphA3<sup>+/−</sup> mice, 5 homozygous EphA3<sup>+/+</sup> mice, and five wild-type mice. The perturbations are restricted to the nasotemporal-rostrocaudal projection which varies primarily azimuthally and the original analysis accordingly generated 1-dimensional mapping profiles along this axis taken along three straight lines drawn through the colliculus which were thought to correspond with iso-elevational lines. For each of the three profiles the correlation coefficient was computed and two indexes were generated as functions of the three correlation coefficients: the linear fit index and intra-map index. These indexes were plotted against each other which revealed clustering of wild-type and homozygous specimens with the heterozygotes distributed between. There are two salient potential issues with this analysis: straight collicular lines do not correspond to iso-elevational contours and the clustering analysis indexes correlate with each other. The first issue may be resolved by realising that each of the image coordinates corresponds to a physical location which can be registered between the elevational and

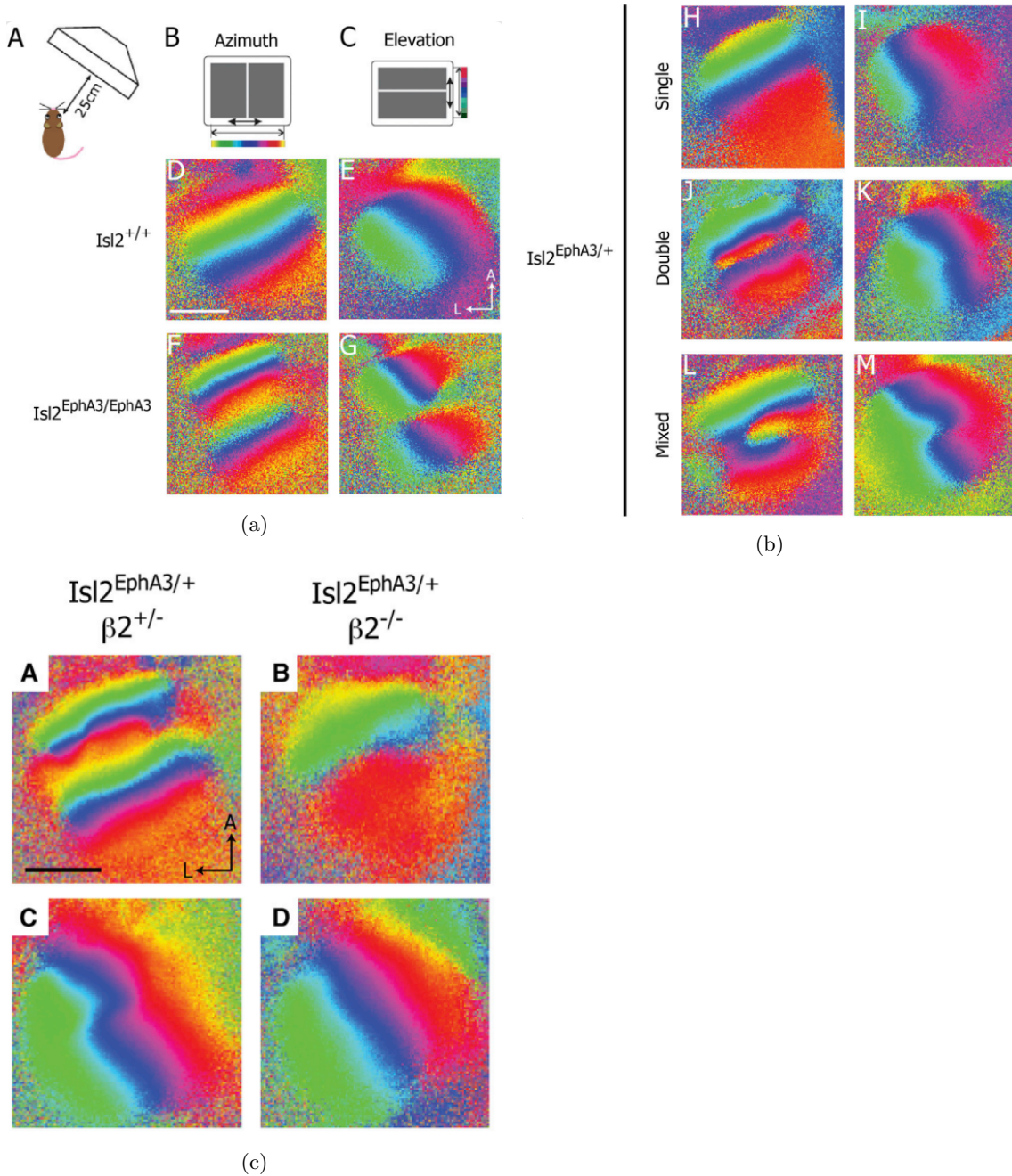


Figure 2.1: The diversity of intrinsic optical imaging scans captured in the Owens et. al. (2015) dataset. Panel (a) demonstrates the experimental set up and present azimuthal (left) and elevational (right) scans for a wild-type and homozygous  $\text{EphA3}^{+/+}$  mutant. The heterozygous  $\text{EphA3}^{+/-}$  mutants are presented in panel (b) and have been subdivided into single, double, and mixed classifications. Finally, panel (c) presents a heterozygous case with unaltered activity patterns (left) contrasted against one with altered activity patterns found in the  $\beta 2$  knock-out mutant. These altered patterns appear to recover retinotopy. .

azimuthal scans and the elevational scan may be used to trace iso-elevational lines. The second issue may potentially not interfere with the end result but cannot be resolved.

To complement this analysis we combined the elevational and azimuthal scans so that each collicular pixel had an associated coordinate in visual space thereby having a datum of the four dimensional topographic object discussed in Section ???. The colliculus region is defined by an ellipse encompassing the region where the stimulus excitation from the visual field is highest [38]. The data then went through two filtering schemes to improve quality. First, the bulk, or average, activity was calculated for each pixel in the collicular region over the time course of the stimulation and the 10000 most active were selected [16]. Second, we calculate the mean phase convolved over a pixel width of 5 and when the standard deviation of this mean is three times greater than the wild-type standard deviation the pixels are rejected. We perform this step because when the stimulus reaches the boundary of a functional map it will be stimulated from two distal retinal locations and thus be highly variable. The phase measurement will be associated with the average position of these two distal locations and it cannot be reliably mapped to either; a problem associated with the subjectivity of the visual-collicular projective map discussed in Section ???. These filtering processes allow us to define a complete topographic map conditioned on the visual stimulus of physical collicular locations. We represent the pixels that constitute these maps in grey, and the pixels that are filtered in green. We also show three curves of iso-elevation in the eligible grey pixels at  $-25^\circ$ ,  $0^\circ$ , and  $25^\circ$  which are represented in orange, cyan, and brown respectively.

With a complete representation of the topographic relationship we can apply the Lattice method of data analysis to each of these datasets discussed in Section ???. We chose a subset of eligible pixels with a mean spacing of 6 pixels or  $80\mu\text{m}$  to tile the colliculus. The spacing between collicular nodes was chosen to be the smallest that gives highly ordered 2D maps in wild-types, as found in an analysis of another data set [74]. The mean visual field of all pixels falling with 3 pixels of these locations was calculated and associated with each location. The tiling was projected to the visual field and any edges found to be crossing were removed and highlighted in red with the resulting map giving a standardised topographic representation of the data: a lattice object. In the case of the heterozygotes and homozygotes and the data may be further subdivided into rostral and colliculus portions by fitting a line through the rejected high variance points (green). Each of these regions can be associated with a part-map or lattice object constructed from pixels only in this region. We show an example of the lattice object generated for a wild-type in Figure 2.2. The variation in the iso-elevational lines indicates a marginal distortion in the dorsal-ventral axes.

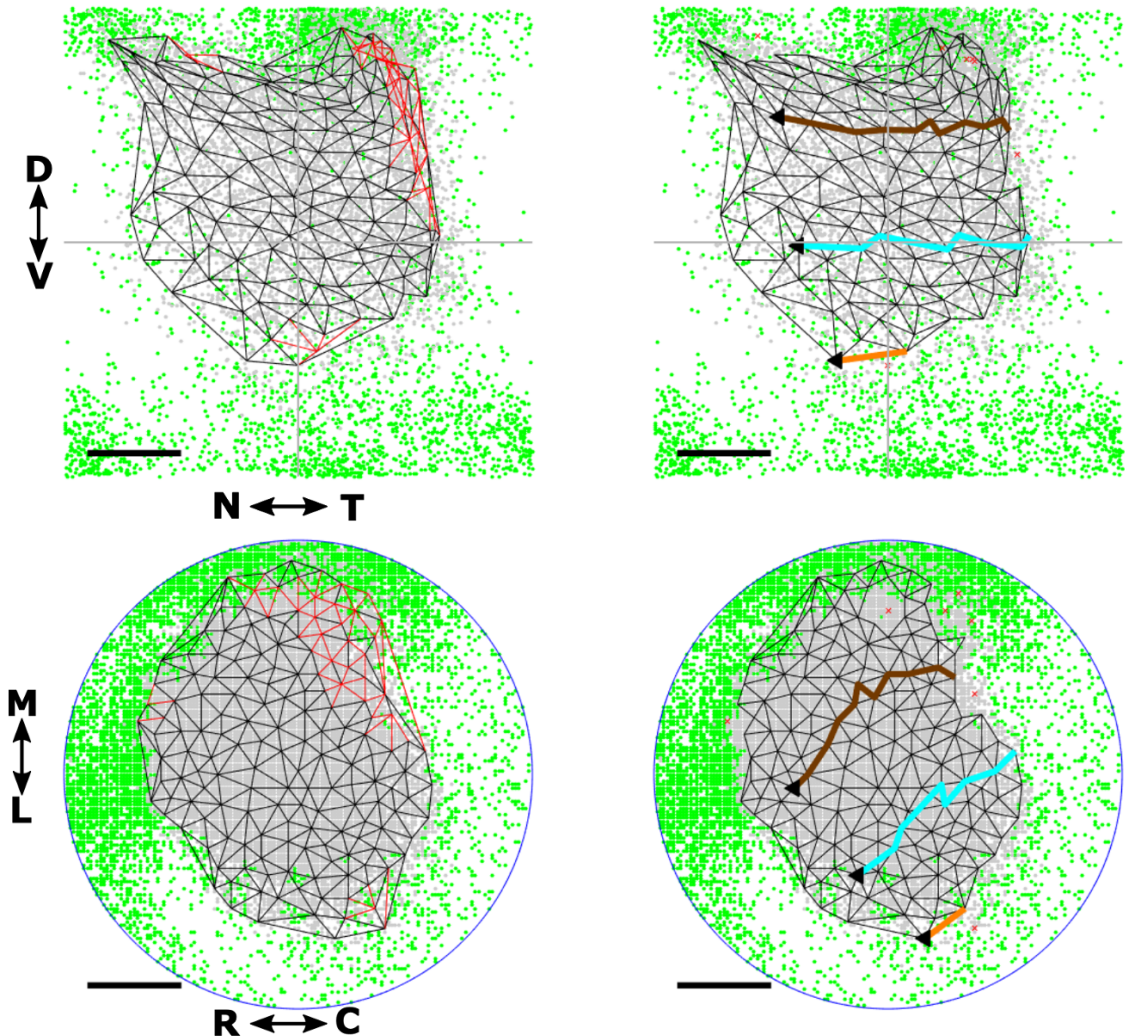


Figure 2.2: An example of a lattice generated from a wild-type dataset. The scale bar is 200um. We draw attention to several conventions in this image. First, the green pixels are filtered data while the grey indicates the retained data. Second, the whole map is presented to the left conventionally while the largest ordered submap is presented to the right. The removed links are highlighted in red in the old map and have a corresponding red cross on the submap. The three iso-elevational lines are represented in brown, cyan and orange. This example represents an excellent local ordering as only 4% of the nodes had to be removed to give the largest ordered submap and high polarity scores.

For each dataset we used the lattice objects to calculate a series of statistics: rostrocaudal and mediolateral polarities, azimuthal and elevational magnification, map quality, and visual field overlap. Rostrocaudal polarity (RCP) is the proportion of edges in the visual representation which project onto the colliculus in the same relative rostrocaudal order as they would in a perfectly ordered map. A score of 100% represents perfect ordering along the rostrocaudal axis, 50% indicates random order and perfect but reversed order is 0%. Mediolateral polarity (MLP) is calculated similarly. Magnification ratio is a measure of the relative extent of the projection along a specified axis. The Azimuthal Magnification (AM) is the length of each edge measured along the rotated nasotemporal axis of visual field compared to the length of the corresponding edge along the ros-

trocaudal axis of the colliculus; similarly for the Elevational Magnification (EM). Map quality refers to the number of nodes which need to be removed in order to form the perfect topographic representation. In cases when two maps were constructed by partitioning the colliculus, the extent of visual field which projects to both regions of the colliculus, called the Visual Field Overlap (VFO), was measured. In a complete double map, the VFO is the entire extent of visual field. We used these statistics to classify the heterozygotes into three categories concordant with the Owens et. al. analysis: A, B, and C. Example maps for these three heterozygotes are shown in Figure 2.3.

The statistics associated with each population are shown in Table 2.1. The rostrocaudal and mediolateral polarities where all in excess of 90% in concordance with wild-type. The HETA classification shows very similar statistical profiles to the wild-type with no visual field overlap being recorded. The HETB specimens are beginning to deviate particularly in VFO. The HETC specimens present more similarly to HOM specimens with similar VFO and map qualities. The azimuthal magnification is distinguished between the two part maps due to the compression of each map into a region of the colliculus. The elevational magnification remains unchanged. The Lattice method has revealed evidence for two part maps in all of the homozygotes and to a lesser degree each of the heterozygotes. These part maps are formed by bisecting the colliculus into two regions on the basis of data quality and when this bisection is made each of the part maps form individual higher quality lattices than the whole map lattice. These higher quality maps can be used to interrogate the coverage of the visual field and in particular the overlap of the visual space covered by each part map: the VFO. These two statistics can be used to classify the heterozygous variability under the following criteria: the part-map subdivision must not substantially improve map quality over the whole map to be classified as similar to wild-type and the VFO must be statistically similar to the homozygous distribution to be classified as a homozygote.

Classification	AM	EM	Quality	VFO
Wild Type	$93 \pm 13^\circ/\text{mm}$	$71 \pm 9^\circ/\text{mm}$	$91 \pm 5\%$	--
HETA	$98 \pm 16^\circ/\text{mm}$	$63 \pm 5^\circ/\text{mm}$	$86 \pm 2\%$	$0 \pm 0\%$
HETB	$xx \pm xx/\text{mm}$	$xx \pm xx/\text{mm}$	$91 \pm 5\%$	$4 \pm 2\%$
HETC	$150(96) \pm 15(10)^\circ/\text{mm}$	$x \pm x$	$70 \pm 10$	$27\% \pm 13\%$
HOM	$203(101) \pm 20(16)^\circ/\text{mm}$	$x \pm x$	$60 \pm 15$	$33\% \pm 18\%$

Table 2.1: Summary statistics based on the lattice analysis. The magnification ratios for each of the part maps are summarised (where appropriate) with the rostral projection and the caudal projection is reported in brackets. The whole map quality is shown to degrade from wild-type to homozygote and the average part map quality is reported in brackets. The VFO increases from wild-type to homozygotes. The VFO and map quality statistics appear to be the most relevant statistics to query whether there is a significant overlap between classifications. These statistics are generated on small samples ( 5 specimens each) and caution should be applied interpreting them.

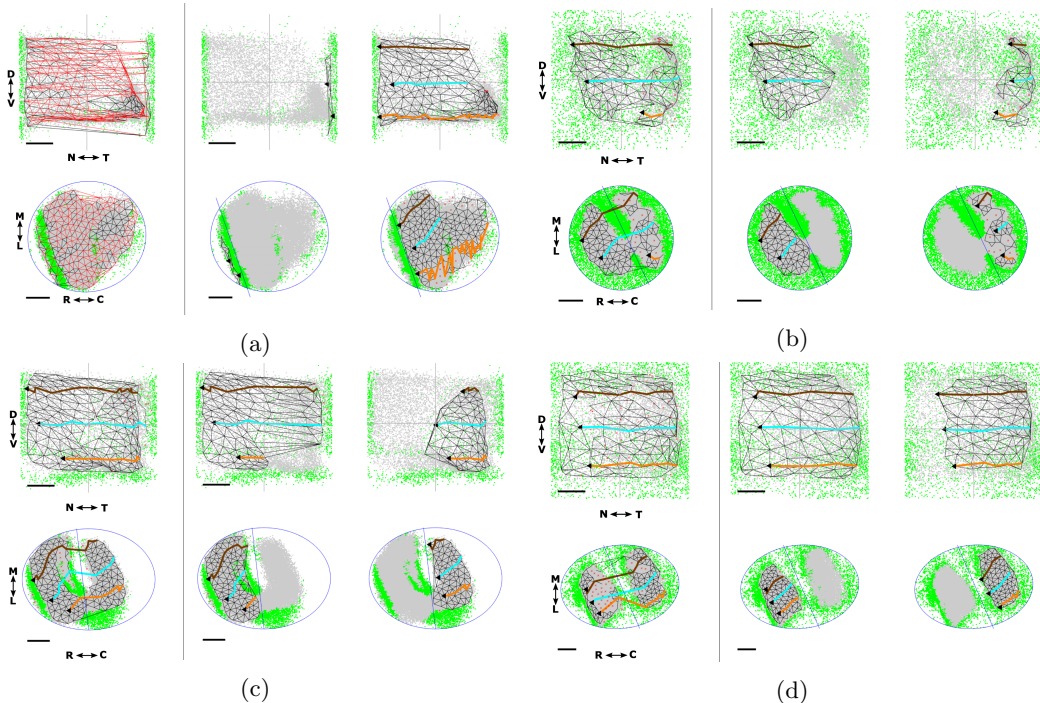


Figure 2.3: Examples for the three heterozygous classifications and the homozygous maps. For each of these maps the whole map lattice is calculated and shown in the left and the rostral and caudal part-maps are shown on the right; the scale bar is 200um.. An example map for the A classification is shown in panel (a) and shows a very small secondary part map with reversed polarity. When the two part-maps are disambiguated the map quality improves with less nodes being removed compared to the whole map and the first part map corresponds well to a wild-type. An example map for the B classification is shown in panel (b) and while the whole map suggests a degree of ordering it is improved by separating the projection at the neck of the eligible pixels in grey. An example map for the C classification is shown in (c) and here map quality is substantially improved by segregation with a complete visual representation rostrally and a partial visual representation caudally; these heterozygotes are qualitatively similar to homozygotes in this respect. An example map of a homozygote is shown in (d) with the eligible pixels completely forming two independent regions and with each of these regions containing a well ordered and substantial portion of the visual field.

## 2.4 Modelling Pipeline

To theoretically analyse the stochastic hypothesis we need to be able to directly compare model output with data elements. There are two key issues here: registration and anatomical interpretation. The lattice method provides a good solution to the first problem as it is defined topologically and therefore we can compare lattice properties such as visual field coverage between two model runs without needing to ensure that all points are metrically registered against each other. The method also allows us to directly compare to the data under the hypothesis that the model generates comparable data-types. This leads us to the second problem which is how precisely are the Tsigankov-Koulakov connections defined. The most reasonable interpretation given the data used to define the models is that they are anatomical, not functional [72, 40, 71, 69]. For the

wild-type phenotype the distinction is irrelevant because the functional imaging scans would be in correspondence with the anatomical retinotopy. However, when there is a duplicated or ectopic connection this association is non-trivial. The phase of the signal will be now composed of several components of the visual field.

To compare the model and data we need to use the model as a network generator on which we can model activity dynamics. We can then simulate the activity induced by the optical imaging paradigm and generate lattice objects on the basis of these activity patterns which are comparable to data. This interpretation confers an additional benefit: the underlying anatomical properties of the network are completely known. We can therefore generate anatomical lattices and make predictions about the underlying structure of maps. This is of particular interest in a related hypothesis of EphA3 homozygous mice: do the wild-type and EphA3<sup>+/+</sup> afferents completely segregate in the colliculus? A review implies that they do but this appears to be based on functional optical imaging scans while anatomical injection studies are too sparse to interpolate on. These questions are intimately related to the role of competition with respect to gradient sensing mechanisms and therefore our choice of model is the Tsigankov-Koulakov model extended to have multiple connections and a competitive sorting mechanism [69].

### 2.4.1 Anatomical Model

We shall briefly detail the model here and it is detailed in full in Section ???. The model is an energy minimization model which assigns energy to a configuration of synaptic connections between a set of collicular and retinal cells. The energy is given by:

$$E = \sum_{p \in \{\alpha, \beta\}} \sum_{i \in \text{syn}} p R(i_{\text{ret}}, p) L(i_{\text{col}}, p) - \frac{\gamma}{2} \sum_{i \in \text{syn}} \sum_{j \in \text{syn}} C(|i - j_{\text{ret}}|) U(|i - j_{\text{col}}|) + \sum_{i \in \text{ret}} (n_i^2 - 500 n_i^{1/2}) + \sum_{i \in \text{col}} n_i^2, \quad (2.1)$$

where  $\alpha = -90$ ,  $\beta = 120$ ,  $C(d) = \exp(-|d|/11)$ ,  $U(d) = \exp(-d^2/18)$ , and  $\gamma = 0.05$ . The model minimizes the energy by allowing for a creation and deletion of synapses. The resulting energy change  $\Delta E$  with either creation or deletion is associated with a probability:

$$p = \frac{1}{1 + \exp(-4\Delta E)}, \quad (2.2)$$

and at each time step the model stochastically samples a possible creation and deletion. We chose to run the model to run for  $5 * N^2$  time-steps where  $N$  is the number of cells in both the colliculus and retina. This allows each potential retinocollicular connection to be sampled on average 5 times and

leads to good convergence. The parameter choices made here follow the paper and Git repository for Hjorth (2015) [34]. However, they diverge from the original model. These parameters have produced good results in this study but it is still prudent to exercise caution about them given that there are no comprehensive studies exploring the parameter space of this model.

For high resolution maps we chose  $N = 10000$  while for low resolution maps which converged quickly we chose  $N = 2000$ . The model was implemented computationally using the MATLAB package developed by Hjorth et. al. (2015) [34] on an AMD Ryzen Threadripper 3950X with 32 cores.

To model the EphA3 systems we chose a number of retinal cells to be tagged as EphA3<sup>+-</sup> cells. To these cells we added an additional  $\Delta R$  to their EphA gradient  $R_A(x)$ . The gradients are normalised to a maximum value of one in the wild-type and it remains an open question what  $\Delta R$  should be equal to. It seems reasonable that the homozygote should be twice that of the heterozygote but this does not follow automatically. In light of this we performed a parameter sweep of  $\Delta R$  to understand its effects in parameter space more generally.

### 2.4.2 Spiking Model of Neural Activity

To simulate activity in the superior colliculus we used a simple Poisson integrate-and-fire model; see Section ???. We assume that each collicular  $i$  cell is connected to each retinal cell  $j$  with a weight  $W_R(i, j)$  given by the output of the anatomical model, and to other collicular cells  $k$  with a weight given by the function of the distance  $d_{ik}$  between them:

$$W_C(i, k) = w_1 \exp\left(-\frac{d_{ik}^2}{2r_1^2}\right) - w_2 \exp\left(-\frac{d_{ik}^2}{2r_2^2}\right), \quad (2.3)$$

where we chose the colliculus length to be normalised to one and  $r_1 = 0.01, r_2 = 0.02, w_1 = 0.02$ , and  $w_2 = 0.01$  to mimic the lateral connectivity pattern reported in the colliculus [55]. We assume that each collicular cell receives input in the form of spikes from retinal cells and other collicular cells and these spikes are integrated over time to form the rate parameter:

$$r_i(t, t_0) = \int_{t_0}^t dt \left( \frac{1}{\sum_j W_R(i, j)} \sum_j W_R(i, j) I_R(j, t) + \frac{1}{\sum_k W_C(i, k)} \sum_k W_C(i, k) I_C(k, t) \right), \quad (2.4)$$

where  $t_0$  is the time of the last collicular spike in  $i$ , and  $I_R(j, t)$  and  $I_C(k, t)$  are the spike trains for retinal index  $j$  and collicular index  $k$  respectively. We chose our sampling rate to be  $dt = 0.01$  seconds and at each timestep  $dt$  we calculate a random number  $p_i$  and generate a spike in collicular

index  $i$  if:

$$r_i(t, t_0)dt < p_i. \quad (2.5)$$

We then keep a record of all collicular spikes and associate this with collicular activity generated by stimulating the retina with a given input pattern  $I_R(j, t)$ .

### 2.4.3 Optical Image Scan Reconstruction

To reconstruct the optical images we follow the procedure in Kalastky and Strkyer (2003) [38]. We apply a wave of stimulus across the retina as input in an orthogonal direction and repeat this with periodic boundary conditions ten times. The activity is propagated into the network model as a series of neuronal spikes generated by a Poisson process and this combined with lateral connectivity generates a series of spikes in the colliculus. The procedure is reversed and two records of the activity in the forward and reverse directions are kept. The entire procedure is again repeated along the complementary orthogonal direction and these are associated with azimuthal and elevational activity. Figure 2.4 shows the phase plots for a wild-type phenotype, Figure 2.6 shows the azimuthal phase plots for heterozygous and homozygous knock-ins. We can now apply the lattice method directly to this surrogate phase data and forward (visual field to colliculus) and reverse (colliculus to visual) field are shown conventionally in blue and black respectively; see Figure 2.7.

## 2.5 Results

We do not know *a priori* what the value of  $\Delta R$  should be to generate a heterozygous or homozygous genotype and we proceed by interrogating a range of values  $\Delta R = \{0.2i\}_{i=0}^{i=10}$  which is analogous to assuming a uniform prior on the  $\Delta R$  parameter. The model is too computationally demanding to perform many runs at  $N = 10000$  and so these results are seeded at a seed number of 1. We will perform several anatomical experiments on these maps, followed by a lattice analysis, before attempting to analyse the statistical properties of these maps at a lower but more computationally manageable resolution.

### 2.5.1 Anatomical Experiments

The model allows us to record the provenance of a synaptic connection: a synapses origin can be labelled as an EphA3 expressing or wild-type cell in the retina. In the following experiments we

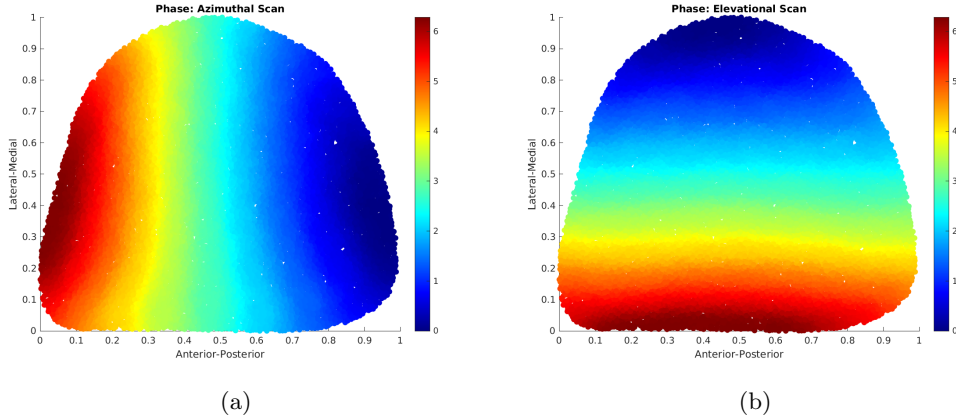


Figure 2.4: We present the azimuthal and elevational phase diagrams for a wild-type simulation in panels (a) and (b) respectively following the procedure outlined Kalatsky and Stryker (2003) [38]. There is a good correspondence between these phases maps and those measured biologically. We take care to remember that biological phase maps are stimulated azimuthally and conventionally and these roughly correspond with the orthogonal gradients in the retina but not precisely, in our maps this relationship is precise but we keep the naming convention.

exploit this by labelling all wild-type cells in red and all EphA3 tagged cells in gold.

We start by performing anterograde injections into the superior colliculus from the retina. We first find the average projection location in the rostrocaudal of all cells within a given tolerance of 1% in the nasal-temporal axis. We also perform the analogous retrograde injection from the colliculus to the retina. These reproduce in a single map the experimental injections performed and averaged over many mice [12]. These results are in accordance with those experiments demonstrating that the model predicts individual map presentations correlate closely with aggregate population maps. These experiments can be seen in the third and fourth rows of Figure 2.5.

We next performed a whole field flood of the retina with red and gold labelled dyes in an experiment analogous to the one performed for the *Math5* mutant [70]. This experiment reveals the volume of the colliculus which each cell type is restricted to. We notice that for low amounts of  $\Delta R$  the populations are fairly well mixed across the colliculus and become increasingly segregated with an increasing level of  $\Delta R$ . For an unobserved level of  $\Delta R = 4$  the maps become completely segregated. These experiments can be seen in the final row of Figure 2.5.

### 2.5.2 Lattice Analysis

We used the anatomical map for each sample of  $\Delta R$  to perform an optical imaging experiment and example azimuthal scans are presented in Figure 2.6. After performing the data filtering procedure used on the biological specimens we generated a number of different lattice objects on both the anatomical and functional maps. The lattices in both directions between visual field/retina and colliculus were generated. For each of the colliculus maps we used the average rostrocaudal location

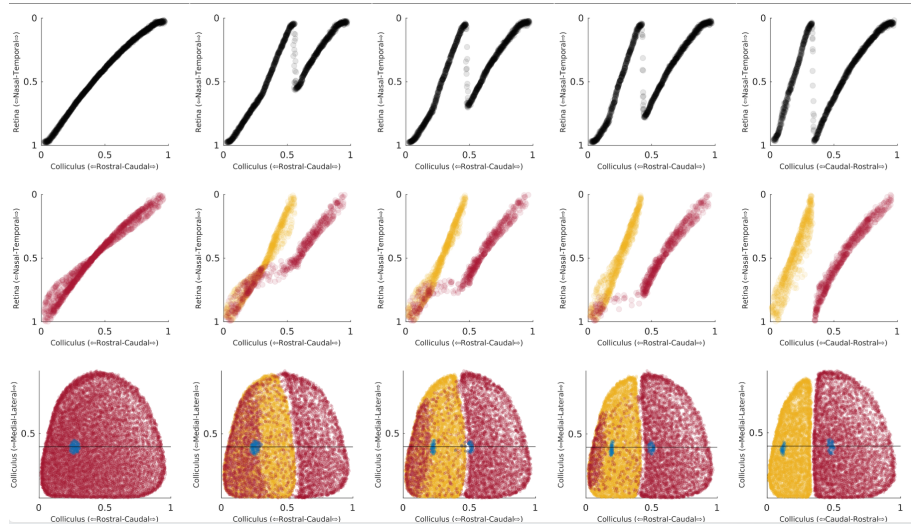


Figure 2.5: A series of injection experiments are performed on knock-in simulations with  $\Delta R$  increasing left to right from  $\Delta R = 0$  (wild-type) to  $\Delta R = 2.0$  (HOM). In each plot the EphA3 projection and cell-type is labelled in gold while the wild-type cell-type is labelled in red. The first row represents the average projection from collicular cells in the rostrocaudal axes to the nasal-temporal axes (colliculus-to-field), the second represents the average projection of the retinal cells into the rostrocaudal axis (field-to-colliculus), and the third represents the retinal providence of each collicular cell. In the colliculus a number of points are highlighted in blue and these correspond to an injection made of 1% of the retina in the central field corresponding to the experiments performed by Brown et. al. (2000) [13].

of the filtered data to generate a discriminator to separate the two functional colliculus maps. The collicular cells in these regions were then used to generate a lattice onto the retina to give an indication of the quality of each of the functional maps. We also performed an analogous experiment in the retina whereby we restricted the mapping to a single cell type and performed another scan to generate the lattice it would have in the absence of interactions with the other cell-type; the additional scan is necessary to remove these interactions.

**Whole-Maps and Part Maps** We highlight the differences between whole maps and part-maps in Figure 2.7. The maps are constructed as projections from colliculus (black) and to colliculus (blue). The removed links in red when constructing the whole map are pervasive and indicate a lower quality map. By subdividing the region into two sections in the colliculus-to-field projection, or by conditioning on the cell type provenance in the field-to-colliculus projection the resulting part-map have a much higher quality. In this HET type simulation this provides evidence for two projections and we use this technique to analyse the effect of varying EphA3 in creating a detectable secondary projection.

**Lattice Analysis of Varying EphA3 magnitude** We present two series of lattices both derived from stimulating the colliculus and then using the associated phase-visual field link proposed by Kalastsky and Stryker (2003) to generate the lattice: the first selects points from the collicu-

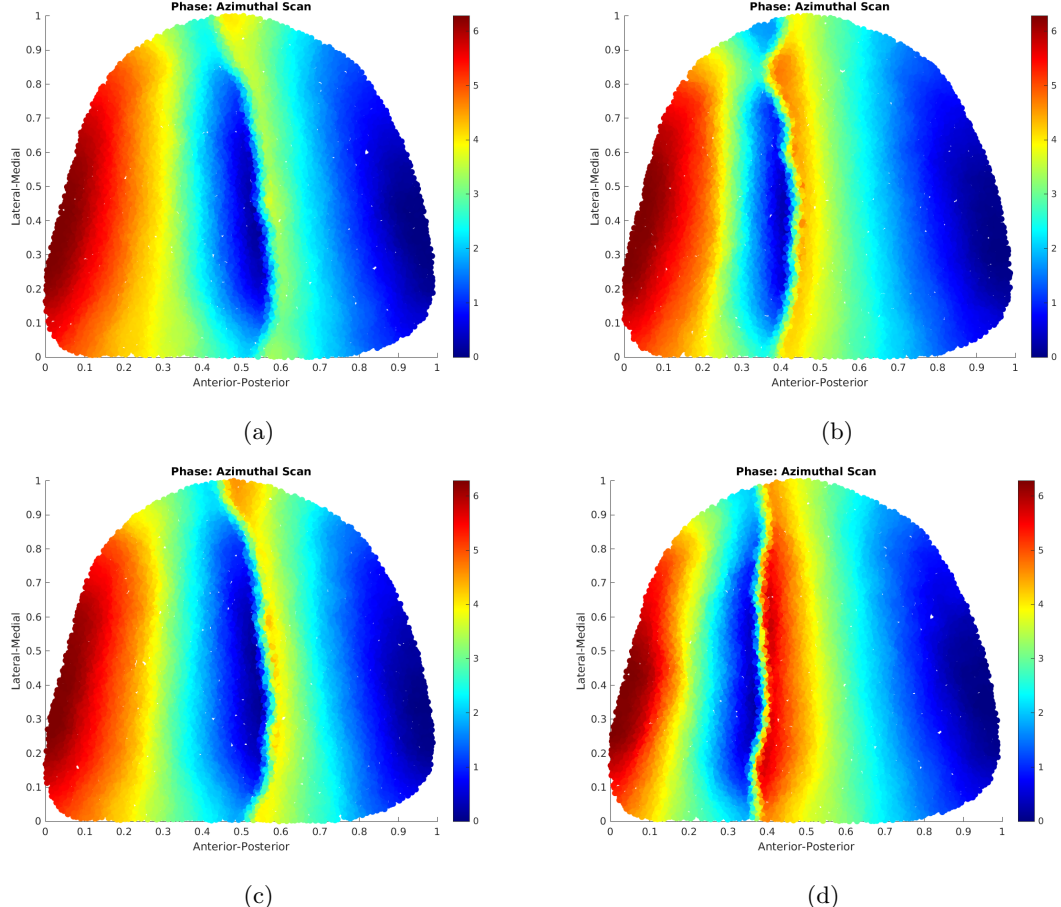


Figure 2.6: We present the azimuthal phase diagrams for several heterozygote simulations and a homozygote simulation. Panel (a) corresponds to  $\Delta R = 0.8$  and resembles a HETA type classification. Panel (b) corresponds to  $\Delta R = 1.0$  and resembles a HETB type classification. Panel (c) corresponds to  $\Delta R = 1.2$  and resembles a HETC type classification. Panel (d) corresponds to  $\Delta R = 2.0$  and resembles a HOM classification. This demonstrates that under choices which correspond to experimentally observed knock-in values the optical imaging procedure can recreate the properties of the functional imaging data in biological specimens [59, 51].

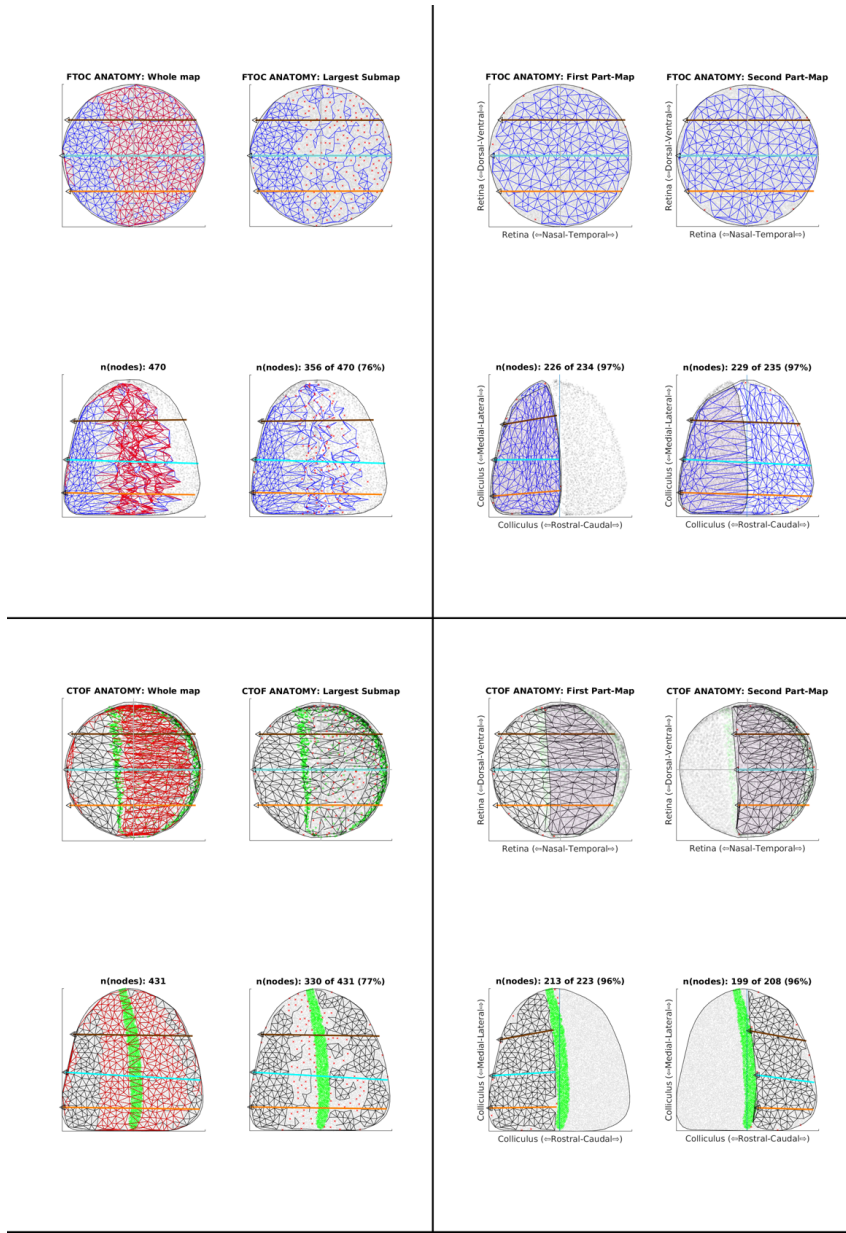


Figure 2.7: A series of whole maps and part-maps generated on anatomical data for a heterozygote type simulation. The blue represents a projection from the field into the colliculus and the part maps are generated by conditioning the pre-image on Islet2-EphA3 and wild-type cells respectively. The black represents a projection from the colliculus to the field and the part maps are derived by segregating the colliculus into rostral and caudal regions using the average location of the filtered points as a discriminant. The remove links in the whole map can be seen in red and the projection overlap is highlighted in purple.

lus and projects into the field, the second projects from the field into the colliculus. To examine the evidence for a second projection appearing with increasing  $\Delta R$  we generate and display the part-map lattices. These lattices are generated in both directions and after filtering are shown in Figure 2.8. In each lattice the projection overlap is presented in purple.

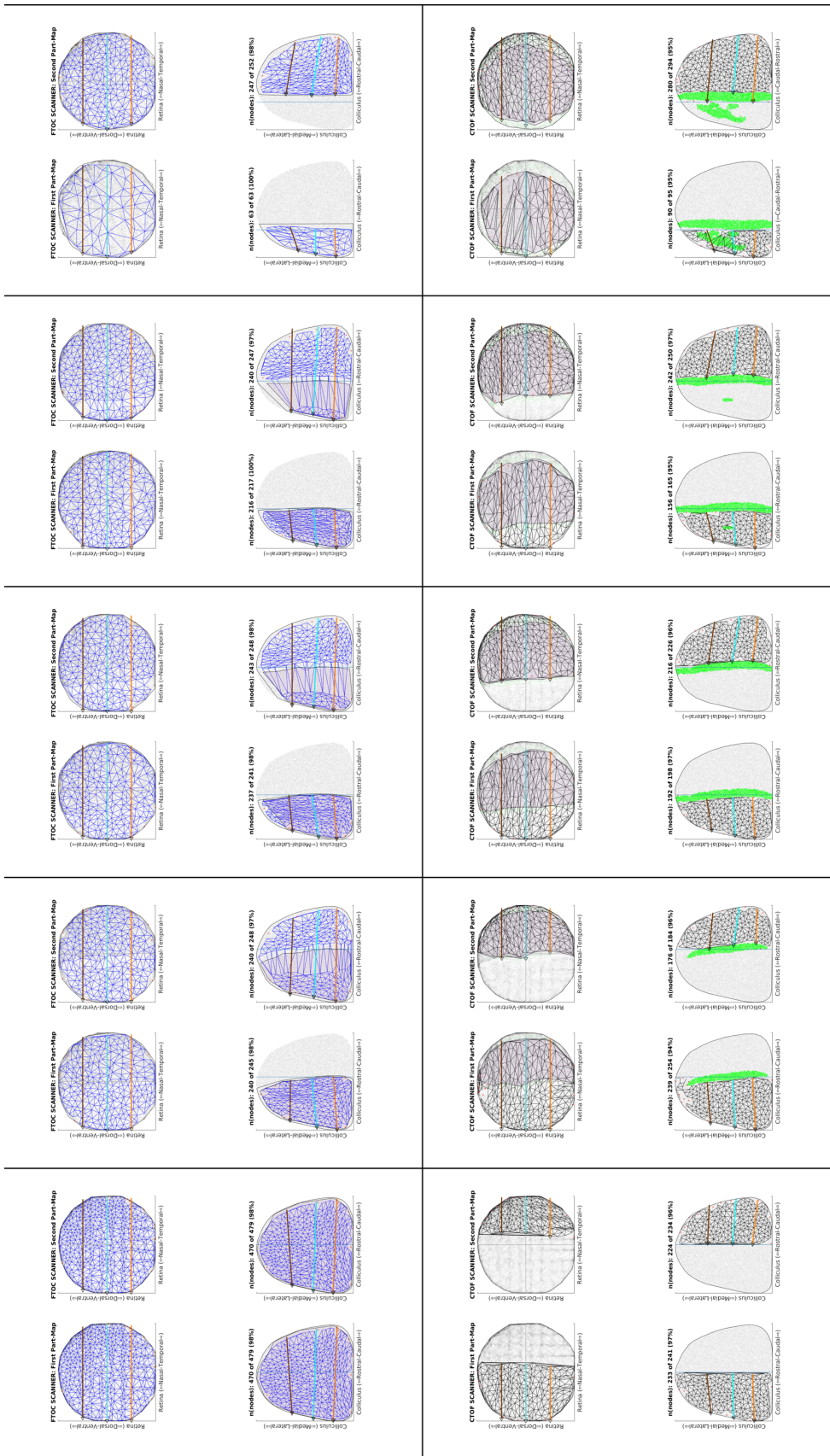


Figure 2.8: Two series of part-map lattices are shown with increasing  $\Delta R$  in steps of 0.4 from left to right. The field-to-colliculus are presented on the top row and several notable features are discussed. First, the distinction between the EphA3 and wild-type projections is apparent in the relative densities of the lattice map that the algorithm generates. Second, the wild-type projection predominately inhabits the caudal region but can be seen to overlap into the far rostral region until very high levels of  $\Delta R$ . The colliculus-to-field maps are shown in the bottom row. The noise introduced by the optical imaging procedure in the region of intermingling maps increases with  $\Delta R$  mimicking what we observe biologically. Both the rostral and caudal regions from a progressively larger cover of the visual field but the rostral region is of slightly lower quality. This is likely due to the compression of the EphA3 projection into the rostral region of the colliculus.

### 2.5.3 Statistical Discrimination of Phenotypes

We have established a generative modelling pipeline with which to query phenotypical presentations of a given genotype. Our principle question is whether the model supports an EphA3 knock value which can present as a homozygous phenotype and wild-type phenotype for different model runs. To assess this it is reasonable to ask whether there are significant differences in a sample lattice summary statistic which would reliably discriminate between a homozygote and wild-type. A useful discriminating statistic is the visual field overlap (VFO). The VFO is computed by segregating the caudal and rostral parts of the colliculus and generating a lattice onto the visual field for both parts and recording the fraction of visual field which is represented in both maps. In the wild type there should be no overlap as the map is injective while in the homozygote the overlap should be 1. If the heterozygotes stochastically present as both of these phenotypes then we can expect a significant overlap in the distributions of the means of the  $\text{EphA3}^{+/-}$  VFO with either the wild-type, homozygotes or both.

Examining statistical hypotheses with this model is challenging due to its computationally demanding minimization procedure. A single run at the resolution of  $N = 10000$  takes approximately 20 hours to converge on a single thread. The search can be distributed but even with hundreds of threads available it is prohibitively costly to examine many parameters. To alleviate the computational burden we reduced the resolution to  $N = 2000$ . We chose to examine a parameter set  $\Delta R = \{0.2i\}_{i=0}^{10}$  and generated a modest sample of 100 maps for each parameter value. We distributed this calculation on 24 process using MATLABs parallel computing environment. The visual field overlap statistics are presented in Figure ?? alongside the map quality for each of the whole and part maps, and the mean projection location of the wild-type and Islet2-EphA3 cells. The visual field overlap is 0 until  $\Delta R = 0.4$  where it starts climbing to a maximal value of 0.9 for  $\Delta R = 2.0$ . The mean projection location of the two cell types are shown in Figure ?? where the two projections can be seen to smoothly separate for increasing  $\Delta R$ . The two projections have a significantly different mean at  $\Delta R = 0.6$ . The whole map and part-map qualities are shown in Figure 2.11 where it is seen that whole map quality begins to rapidly deteriorate at  $\Delta R = 0.8$  and the part map qualities initially decrease before recovering to levels of approximately 90%. The statistics run in tandem and become significant discrimination tools at  $\Delta R > 0.8$  corresponding well with the measured value of  $\Delta R \approx 0.8$  [34].

Notably, the collicular overlap does not have a dependence on  $\Delta R$ . Whole map quality decreases with an increasing  $\Delta R$  but can be restored by subdividing the colliculus into two part maps which is in line with our data analysis. The mean projection of each of the two cell types smoothly deforms away from the other.

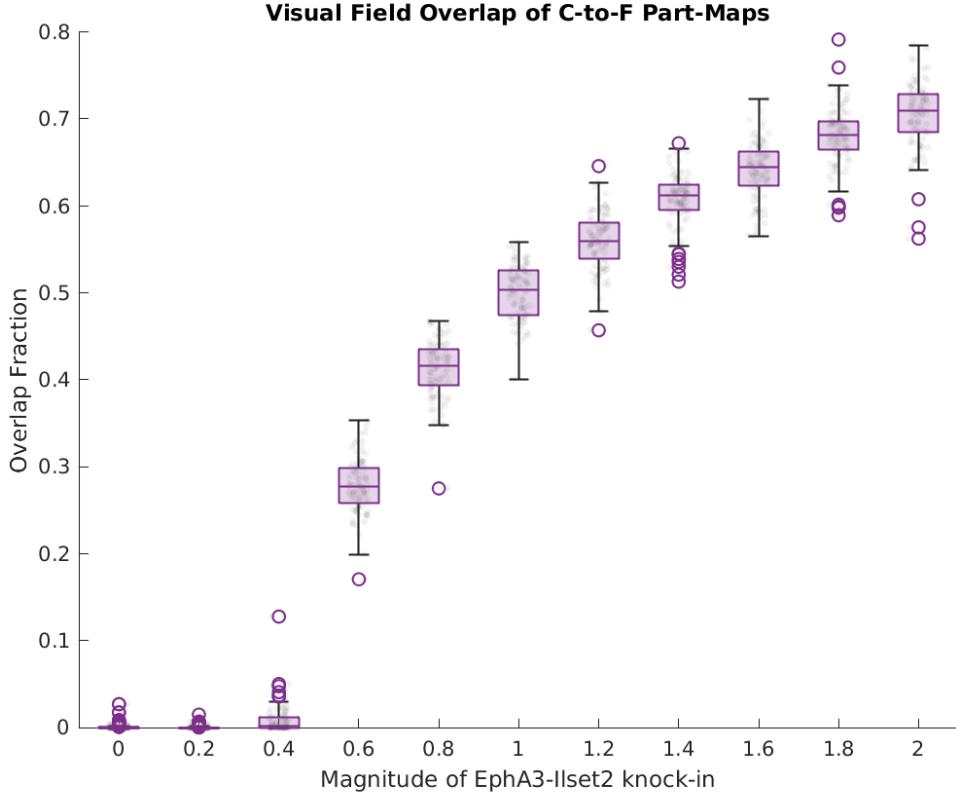


Figure 2.9: The VFO distributions are shown as a function of increasing EphA3. There is a notable critical value at approximately  $\Delta R = 0.2$  to  $\Delta R = 0.4$  where the VFO becomes non-zero. It then smoothly increases up to a value of 0.8 at the homozygous level of  $\Delta R = 2.0$ . The distributions imply that at the experimentally measured levels of EphA3 knock-in for homozygotes and heterozygotes it is not likely that they can come from the same distribution.

#### 2.5.4 Activity Perturbations

We examined the effects of manipulating activity on the bulk anatomical projection. The first series of experiments involved increasing the  $\gamma$  parameter by an order of magnitude to 0.0625 indicating a more prominent role for activity with the result of collapsing all maps into a wild-type phenotype shown in Figure ??a. The second series of experiments involved decreasing  $\gamma$  by an order of magnitude to 0.000625 which had the effect of collapsing low  $\Delta R$  into a single map while reversing the polarity of the Islet2 expressing population shown in gold in Figure 2.12b. Finally, we set  $\gamma = 0.000625$  and widened the correlation window  $b_{act}$  to 0.2 mimicking the correlation results measured for the  $\beta 2$  mutant [66]. The effect of this shown in Figure 2.12c. was to maintain the broad structure of the phenotypic presentation for each  $\Delta R$  while widening the receptive field at each location.

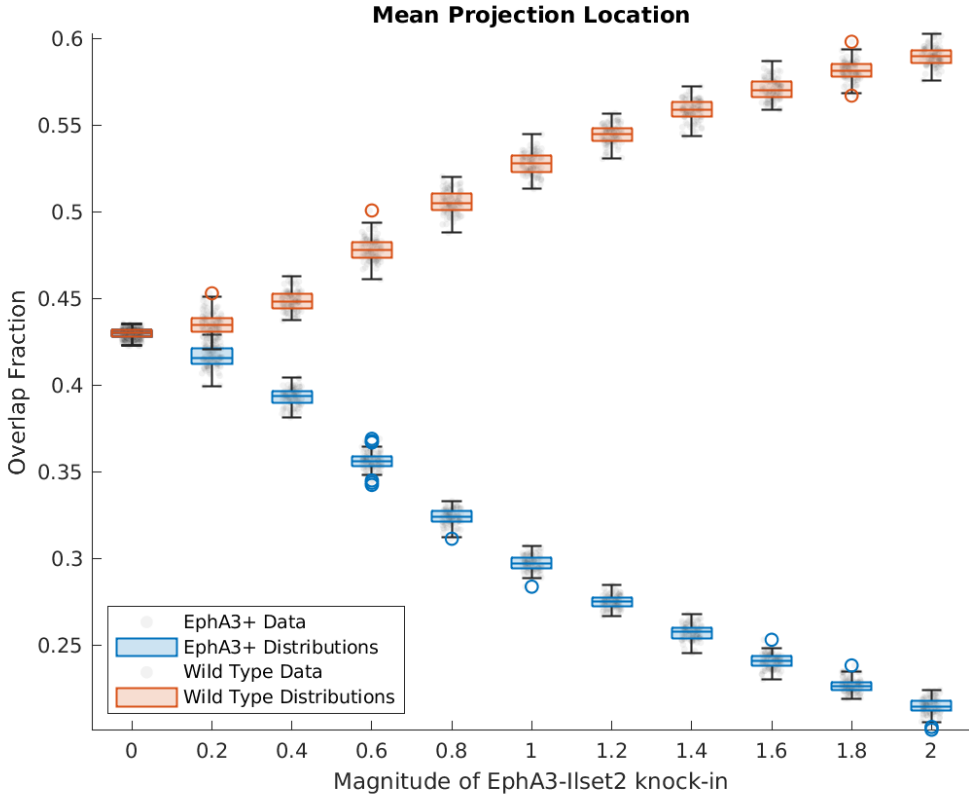


Figure 2.10: The distribution for the mean projection location of each cell type as an increasing function of  $\Delta R$ . The projections can be seen to immediately separate and become significantly different at  $\Delta R = 0.6$ . This validates the VFO as a measurement to discriminate the existence of two projections.

## 2.6 Discussion

The data we have presented here gives us qualitative and quantitative measures by which to benchmark our model analyses. The variability observed by Owens et. al. (2015) has been broken into subclasses which have validated their observations. The model is able to reproduce optical imaging experiments and maps qualitatively as well as key phenomenological features. It reproduces faithful representations of magnification effects but we do not observe any reversal of polarity in any part maps. If we assume the means are distributed normally then the distributions generated by the model are most similar to the HET classes of data in the range 0.4-0.6 under both the map quality and VFO statistics. The HOM class is more challenging to interpret with map quality being most similar to the distributions in the upper limits of the  $\Delta R$  range but with VFO being most similar in the range 0.6-0.8. This challenges the observations of the phase maps which give the best qualitative matches in the range 0.8 – 1.2 for the heterozygotes and 1.8 – 2.0 for the homozygotes and these values are more consistent with previous modelling estimates. The mismatch between the level predict qualitatively by visual inspection of the phase map and

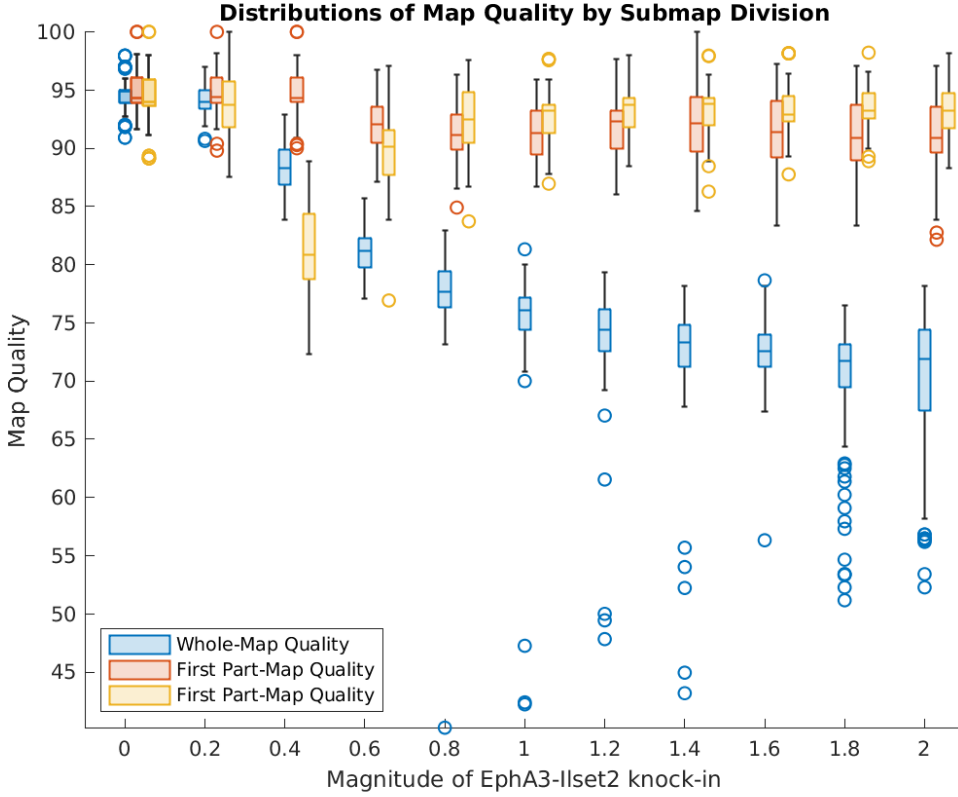


Figure 2.11: The distributions for the whole and individual part maps are shown in blue, red, and yellow respectively. The whole map quality begins to deteriorate at  $\Delta R = 0.4$  and is significantly different from the part maps at  $\Delta R = 0.8$ . The whole map quality continues to decrease with increasing  $\Delta R$  while the part maps remain relatively high quality for  $\Delta R > 0.8$ . The part-map quality returning to 90% is quantitatively in line with the measured values for wild-type maps and part-maps biologically. This supports the existence of two distinct projections for  $\Delta R > 0.8$  which corresponds well to the experimentally measured values for the additional knock-in EphA3 [34].

quantitatively by measured statistics warrants further investigation. There are two principle areas of concern: data number and model resolution. The number of specimens examined were very low, 15 for the HOM class, and it is unlikely that this formed a representative sample. The model resolution used to generate the theoretical distribution was reduced by a factor of 5 for reasons of computational efficiency and this low resolution may mar the predicted distributions; there are notably more outliers for higher  $\Delta R$ . We therefore conclude that the model provides an adequate representation of the biological data conditioned on the low sample number and turn our discussion to theoretical implications.

**Proportion of EphA3 Cells** For each of the  $\Delta R$  experiments we also varied the number of the proportion of EphA3 cells between 40%, 50% and 60%. These experiments do not affect the principle results and have been omitted for this chapter but may be found at [25]. In brief, the effect of increasing the number of EphA3 cells is to increase the volume of the superior colliculus

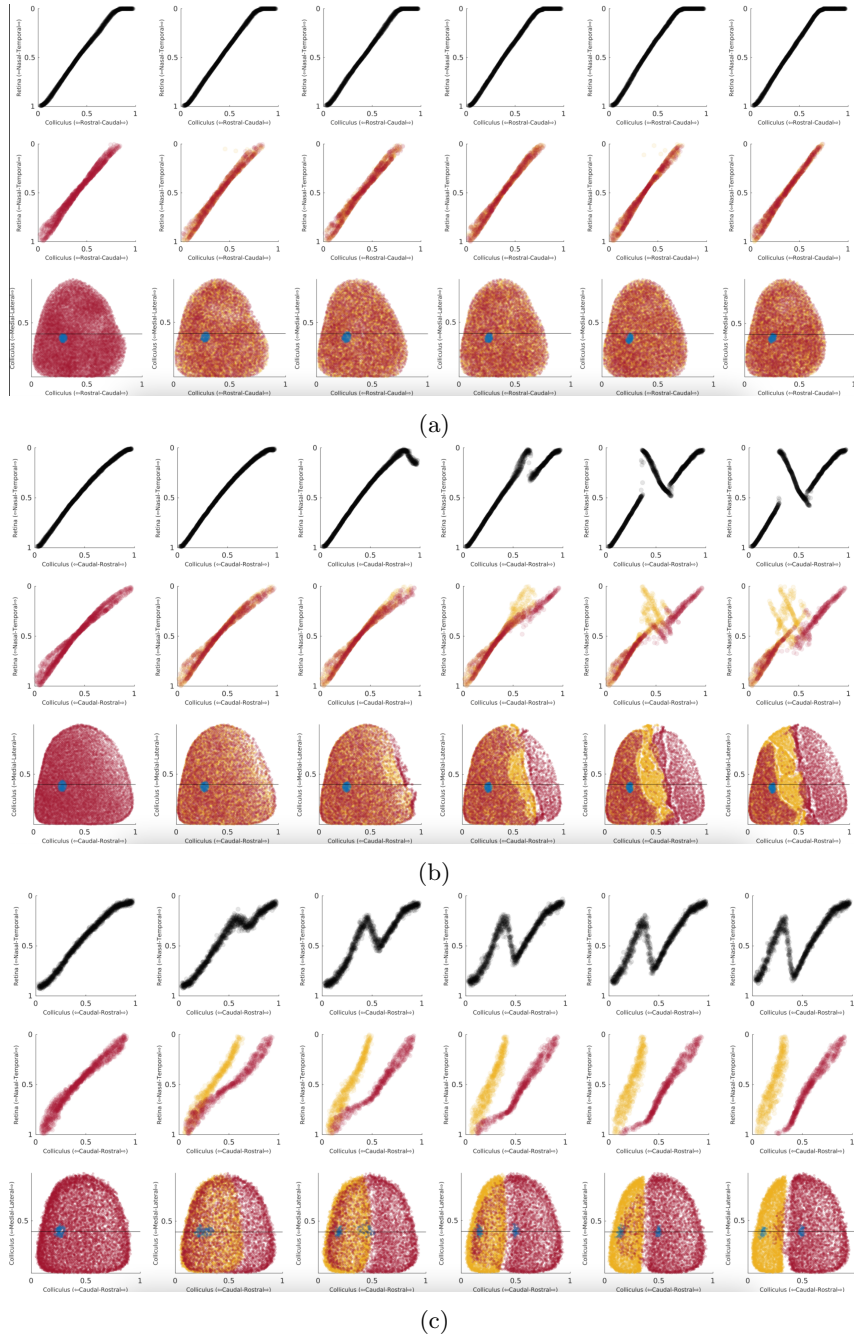


Figure 2.12: A series of injection experiments are performed on knock-in simulations with  $\Delta R$  increasing left to right from  $\Delta R = 0$  (wild-type) to  $\Delta R = 2.0$  (HOM). The result of increasing the strength of activity relationships by setting  $\gamma = 0.0625$  is shown in panel (a) and demonstrates a complete map collapse to the wild-type phenotype. Panel (b) shows that when the activity is downregulated to  $\gamma = 0.000625$  there are reversals in polarity for high  $\Delta R$  and map collapse for low  $\Delta R$ . The effect of mimicking the  $\beta 2$  correlation profile is shown in panel (c) and shows the map phenotypes are maintained but receptive fields are widened.

which they occupy.

**Activity Modelling** Modelling the effect of the  $\beta 2$  perturbations to activity is non-trivial. Recent studies suggest that in the Tsigankov-Koulakov model the chemical cues must be scaled in tandem with the activity cues [45]. For this reason we have primarily focused on modelling the  $\beta 2$  expressing variant for which the Tsigankov-Koulakov model has been validated, and indeed designed for. We performed two pilot studies modifying the scale of activity ( $\gamma$ ) but not the correlation width and the results suggest that regular retinotopy can be recovered if the activity is dominant but lowering the activity results in a collapse into wild-type phenotypes for low  $\Delta R$  in support of the principle hypothesis but maps with disordered polarity for high  $\Delta R$ ; see Figure 2.12. When the activity strength was lowered and the correlation window was widened this effect went away and the map phenotypes remained the same profile as those with normal activity patterns but with widened receptive fields. This is consistent with the general hypothesis that chemotaxis establishes broad topographic patterns and neural activity refines these with the  $\beta 2$  knock-out have less refining capability.

We could not rigorously test this due to a lack of available data but in the context of the reported effects this suggests that the activity strength is significantly increased in the  $\beta 2$  knock-out which is would be a departure from the consensus in the literature [66]. We have not included the lattice plots for these experiments as they are consistent with the interpretations drawn from the anatomy. A potential explanation for the observation of wild-type phenotypes in EphA3 $^{+/-}$  $\beta 2^{-/-}$  mice is that the retinal arbours are simply not refined enough to be phase differentiated. The optical imaging process involves a convolution over the projection of each retinal afferent and injection experiments show that in  $\beta 2$  this projection is a significant portion of the colliculus [48, 14]. This means the phases will be averaged out over large areas and will only distinguish slight biases between each boundary. This hypothesis is consistent with visual inspection of the data but due to a lack of quantitative data we are unable to test it rigorously. It is clear that the activity-chemotaxis interplay alters map formation but modelling cannot reconcile nor reproduce the effect shown by Owens et. al. (2015) in the context of the current parameter space and with available activity profiles [51].

**Anatomical Segregation** We observed that the anatomical region which each EphA3 cell is bound is a smooth function of  $\Delta R$ . The wild-type cells have a more complicated relationship and appear to consistently attempt to project over the whole colliculus and are slowly removed from the EphA3 domain with increasing  $\Delta R$ . At extremely high  $\Delta R = 4$  the populations are completely segregated implying the two functional domains observed have been formed of two analogously cell

differentiated anatomical maps [15]. However, the EphA gradient is normalised to take a maximal value of 1 and data reported from mRNA expression suggests that the additional EphA contributes approximately 1.86 of the maximal value in homozygotes and 0.86 in heterozygotes [59]. At these levels the model does not predict a complete anatomical segregation of the two populations but rather a well defined and constrained EphA3 map restricted to the caudal region and a wild-type map which covers the whole colliculus but has significantly lower coverage in the EphA3 dominated region. We also observe that through this parameter sweep the EphA3 dominated region is well conserved and smoothly deforms to the final segregated state which is evidence that the maps are not stochastically organising individual domains but rather that aberrations in the phase map are derived from phase analysis artefacts from interacting signals with differing retinal provenance.

**Lattice Analysis** The Lattice method gives us a topological insight into how the EphA3 projection is deformed from wild-type to homozygote with increasing  $\Delta R$ . The lattice plots show that this deformation happens smoothly with two maps being developed on top of each other. The maps slowly segregate and as they do they compete less with each other and develop strong complete representations of the visual field.

The two representations can be identified and classified as rostral or caudal on the basis of activity variability under stimulation. This correlates well with the observed data used to construct the maps and can be used to make a direct comparison. By computing the VFO statistics on both the model and data we can gain a measure of the deformation and how it compares with the data. In the model the deformation is relatively smooth with increasing  $\Delta R$ ; see Figure 2.9.

**Variability in the EphA3 knock-in** The above considerations allow us to comment on the variability and anatomy of the EphA3 mutant both in the heterozygote and homozygote case. In the heterozygote case the data shows a large degree of variability in the optical imaging scans which our model has been able to reproduce qualitatively. The source of this variability is unlikely to be the anatomy as our results show the two anatomical projections are reasonably smoothly deformed and well constrained in the colliculus. If the variability were to come from the amount of EphA3 present in the Islet2 expressing cells then there would be a large range of potential EphA3 inserted stochastically between each individual specimen. Then we would be able to see significant VFO overlap between HET, HOM, and wild-type classifications. This seems unreasonable in the context of the measured EphA3 knock-in levels [59]. This leaves only the variability in the signal. Given the noise present in the data and the requirement to filter out large portions of colliculus we can conclude that the overlapping anatomical projections and stochastic processes involved with

the signal generation interact to generate the phase aberrations seen in the data. There will of course be anatomical variations which lead to different signal interactions but the developmental process is not largely stochastic and is instead well ordered.

This argument also allows us to comment on the likely anatomy of the EphA3 homozygote which has been argued to completely segregate in the colliculus [15]. The whole field injections demonstrate that for complete segregation of the Islet2-EphA3 and wild-type cells the EphA3 knock-in must be more than double the maximal value of the regular EphA gradient. This seems unlikely given the measured EphA3 knock-in value derived from mRNA expression levels [59]. The optical imaging pipeline suggests that anatomical segregation is not a requirement for an measured functional duplication; see Figure 2.6. If the Islet2 and wild-type cells can be differentially colour tagged with fluorescent proteins the model predicts a flood injection would reveal wild-type projections in the caudal region occupied predominately by EphA3 type cells. This is an experimentally falsifiable hypothesis and it would be interesting to validate the model against the data in this regard.

**Future Work** We were able to perform a basic parameter search and gain an understanding of the statistical properties of EphA3 knock-in perturbations. To do this we had to exploit access to a high-performance computing cluster and simultaneously had to reduce the resolution of the model thereby reducing its explanatory power. These limitations were imposed by the computationally demanding minimisation procedure employed by the model. In addition, the model parameters were tuned by hand which is useful for exploration but is not scientifically desirable; particularly since the model is a universal function generator. A more rigorous approach would be defining the parameters via Bayesian regression on the available data which would allow us to encode our current prior beliefs; such an analysis was performed in Chapter ???. This approach is entirely unfeasible even with massive parallelisation: the wall time of a single run at high resolution is approximately 20 hours and thousands of runs would be needed for an MCMC to converge [28]. This procedure would allow the data to dictate the relative strength of activity and chemotaxis which is not currently biologically measurable and this relative strength would more rigorously guide theoretical investigations of the interactions between these two mechanisms. It is therefore desirable to design a framework which is computationally efficient enough to be amenable to rigorous parameter and data analysis while maintaining the phenomenological account of the various genotypes. A procedure for assessing the second criteria was given by Hjorth et. al. (2015) [34]. The principles embodied in existing models and outlined in Section ?? will be used in the next chapter to develop a modelling framework that is computationally efficient.

## **Chapter 3**

# **Concluding Remarks and Future Work**

# References

- [1] Ephs, ephrins, and bidirectional signaling. <https://www.nature.com/scitable/topicpage/ephs-ephrins-and-bidirectional-signaling-14749010>  
Accessed: 2021-11-22.
- [2] Essentials of cell biology. <https://www.nature.com/scitable/ebooks/essentials-of-cell-biology-14749010>  
Accessed: 2022-1-7.
- [3] L. F. Abbott and S. B. Nelson. Synaptic plasticity: taming the beast. *Nat. Neurosci.*, 3 Suppl: 1178–1183, Nov. 2000.
- [4] J. B. Ackman, T. J. Burbridge, and M. C. Crair. Retinal waves coordinate patterned activity throughout the developing visual system. *Nature*, 490(7419):219–225, Oct. 2012.
- [5] M. Adli. The CRISPR tool kit for genome editing and beyond. *Nat. Commun.*, 9(1):1–13, May 2018.
- [6] B. Alberts, A. Johnson, J. Lewis, M. Raff, K. Roberts, and P. Walter. *Molecular Biology of the Cell*. Garland Science, 2002.
- [7] T. Baden, P. Berens, K. Franke, M. Román Rosón, M. Bethge, and T. Euler. The functional diversity of retinal ganglion cells in the mouse. *Nature*, 529(7586):345–350, Jan. 2016.
- [8] A. Bansal, J. H. Singer, B. J. Hwang, W. Xu, A. Beaudet, and M. B. Feller. Mice lacking specific nicotinic acetylcholine receptor subunits exhibit dramatically altered spontaneous activity patterns and reveal a limited role for retinal waves in forming ON and OFF circuits in the inner retina. *J. Neurosci.*, 20(20):7672–7681, Oct. 2000.
- [9] M. P. Beckmann, D. P. Cerretti, P. Baum, T. Vanden Bos, L. James, T. Farrah, C. Kozlosky, T. Hollingsworth, H. Shilling, and E. Maraskovsky. Molecular characterization of a family of ligands for eph-related tyrosine kinase receptors. *EMBO J.*, 13(16):3757–3762, Aug. 1994.
- [10] J. A. Bednar and S. P. Wilson. Cortical maps. *Neuroscientist*, 22(6):604–617, Dec. 2016.
- [11] A. A. Boulton, G. B. Baker, and C. H. Vanderwolf. *Neurophysiological Techniques: Applications to Neural Systems*. Humana Press, 1990.

- [12] A. Brown, P. A. Yates, P. Burrola, D. Ortuño, A. Vaidya, T. M. Jessell, S. L. Pfaff, D. D. O’Leary, and G. Lemke. Topographic mapping from the retina to the midbrain is controlled by relative but not absolute levels of EphA receptor signaling. *Cell*, 102(1):77–88, July 2000.
- [13] A. Brown, P. A. Yates, P. Burrola, D. Ortuño, A. Vaidya, T. M. Jessell, S. L. Pfaff, D. D. O’Leary, and G. Lemke. Topographic mapping from the retina to the midbrain is controlled by relative but not absolute levels of epha receptor signaling. *Cell*, 102(1):77–88, 2000.
- [14] T. J. Burbridge, H.-P. Xu, J. B. Ackman, X. Ge, Y. Zhang, M.-J. Ye, Z. J. Zhou, J. Xu, A. Contractor, and M. C. Crair. Visual circuit development requires patterned activity mediated by retinal acetylcholine receptors. *Neuron*, 84(5):1049–1064, Dec. 2014.
- [15] J. Cang and D. A. Feldheim. Developmental mechanisms of topographic map formation and alignment. *Annu. Rev. Neurosci.*, 36:51–77, July 2013.
- [16] J. Cang, L. Wang, M. P. Stryker, and D. A. Feldheim. Roles of ephrin-as and structured activity in the development of functional maps in the superior colliculus. *J. Neurosci.*, 28(43):11015–11023, Oct. 2008.
- [17] A. R. Chandrasekaran, D. T. Plas, E. Gonzalez, and M. C. Crair. Evidence for an instructive role of retinal activity in retinotopic map refinement in the superior colliculus of the mouse. *J. Neurosci.*, 25(29):6929–6938, July 2005.
- [18] S. Chen, M. Zhao, G. Wu, C. Yao, and J. Zhang. Recent advances in morphological cell image analysis. *Comput. Math. Methods Med.*, 2012:101536, Jan. 2012.
- [19] W. Denk, J. H. Strickler, and W. W. Webb. Two-photon laser scanning fluorescence microscopy. *Science*, 248(4951):73–76, Apr. 1990.
- [20] A. Doyle, M. P. McGarry, N. A. Lee, and J. J. Lee. The construction of transgenic and gene knockout/knockin mouse models of human disease. *Transgenic Res.*, 21(2):327–349, Apr. 2012.
- [21] U. C. Dräger and J. F. Olsen. Origins of crossed and uncrossed retinal projections in pigmented and albino mice. *J. Comp. Neurol.*, 191(3):383–412, June 1980.
- [22] D. A. Feldheim, Y. I. Kim, A. D. Bergemann, J. Frisén, M. Barbacid, and J. G. Flanagan. Genetic analysis of ephrin-a2 and ephrin-a5 shows their requirement in multiple aspects of retinocollicular mapping. *Neuron*, 25(3):563–574, Mar. 2000.
- [23] K. C. Flynn. The cytoskeleton and neurite initiation. *Bioarchitecture*, 3(4):86–109, July 2013.

- [24] J. Frisen, P. A. Yates, T. McLaughlin, G. C. Friedman, D. D. M. O’Leary, and M. Barbacid. Ephrin-a5 (al-1/rags) is essential for proper retinal axon guidance and topographic mapping in the mammalian visual system. *Neuron*, 20(2):235–243, Feb. 1998.
- [25] N. Gale. Distributed topographic kernels, 2021.
- [26] N. W. Gale, S. J. Holland, D. M. Valenzuela, A. Flenniken, L. Pan, T. E. Ryan, M. Henkemeyer, K. Strebhardt, H. Hirai, D. G. Wilkinson, T. Pawson, S. Davis, and G. D. Yancopoulos. Eph receptors and ligands comprise two major specificity subclasses and are reciprocally compartmentalized during embryogenesis. *Neuron*, 17(1):9–19, July 1996.
- [27] S. D. Gale and G. J. Murphy. Distinct representation and distribution of visual information by specific cell types in mouse superficial superior colliculus. *J. Neurosci.*, 34(40):13458–13471, Oct. 2014.
- [28] A. Gelman, J. B. Carlin, H. S. Stern, and D. B. Rubin. *Bayesian data analysis*. Chapman and Hall/CRC, 1995.
- [29] C. Grienberger and A. Konnerth. Imaging calcium in neurons. *Neuron*, 73(5):862–885, Mar. 2012.
- [30] E. Herrera, L. Brown, J. Aruga, R. A. Rachel, G. Dolen, K. Mikoshiba, S. Brown, and C. A. Mason. Zic2 patterns binocular vision by specifying the uncrossed retinal projection. *Cell*, 114(5):545–557, Sept. 2003.
- [31] J.-P. Himanen, M. J. Chumley, M. Lackmann, C. Li, W. A. Barton, P. D. Jeffrey, C. Vearing, D. Geleick, D. A. Feldheim, A. W. Boyd, M. Henkemeyer, and D. B. Nikolov. Repelling class discrimination: ephrin-a5 binds to and activates EphB2 receptor signaling. *Nat. Neurosci.*, 7(5):501–509, May 2004.
- [32] R. Hindges, T. McLaughlin, N. Genoud, M. Henkemeyer, and D. D. M. O’Leary. EphB forward signaling controls directional branch extension and arborization required for dorsal-ventral retinotopic mapping. *Neuron*, 35(3):475–487, Aug. 2002.
- [33] H. Hirai, Y. Maru, K. Hagiwara, J. Nishida, and F. Takaku. A novel putative tyrosine kinase receptor encoded by the eph gene. *Science*, 238(4834):1717–1720, Dec. 1987.
- [34] J. J. J. Hjorth, D. C. Sterratt, C. S. Cutts, D. J. Willshaw, and S. J. Eglen. Quantitative assessment of computational models for retinotopic map formation. *Dev. Neurobiol.*, 75(6):641–666, June 2015.
- [35] M. G. Honig and R. I. Hume. Dil and dio: versatile fluorescent dyes for neuronal labelling and pathway tracing. *Trends Neurosci.*, 12(9):333–5, 340–1, Sept. 1989.

- [36] S. Inoué. Foundations of confocal scanned imaging in light microscopy. In J. B. Pawley, editor, *Handbook Of Biological Confocal Microscopy*, pages 1–19. Springer US, Boston, MA, 2006.
- [37] S. Ito and D. A. Feldheim. The mouse superior colliculus: An emerging model for studying circuit formation and function. *Front. Neural Circuits*, 12:10, Feb. 2018.
- [38] V. A. Kalatsky and M. P. Stryker. New paradigm for optical imaging: temporally encoded maps of intrinsic signal. *Neuron*, 38(4):529–545, May 2003.
- [39] S. M. Koch, C. G. Dela Cruz, T. S. Hnasko, R. H. Edwards, A. D. Huberman, and E. M. Ullian. Pathway-specific genetic attenuation of glutamate release alters select features of competition-based visual circuit refinement. *Neuron*, 71(2):235–242, July 2011.
- [40] A. A. Koulakov and D. N. Tsigankov. A stochastic model for retinocollicular map development. *BMC Neurosci.*, 5:30, Aug. 2004.
- [41] T. R. Kumar, M. Larson, H. Wang, J. McDermott, and I. Bronshteyn. Transgenic mouse technology: principles and methods. *Methods Mol. Biol.*, 590:335–362, 2009.
- [42] D. T. Lee and B. J. Schachter. Two algorithms for constructing a delaunay triangulation. *International Journal of Computer & Information Sciences*, 9(3):219–242, June 1980.
- [43] S. R. Lehky and T. J. Sejnowski. Network model of shape-from-shading: neural function arises from both receptive and projective fields. *Nature*, 333(6172):452–454, June 1988.
- [44] G. Lemke and M. Reber. Retinotectal mapping: new insights from molecular genetics. *Annu. Rev. Cell Dev. Biol.*, 21:551–580, 2005.
- [45] D. Lyngholm, D. C. Sterratt, J. J. Johannes Hjorth, D. J. Willshaw, S. J. Eglen, and I. D. Thompson. Measuring and modelling the emergence of order in the mouse retinocollicular projection. July 2019.
- [46] R. C. Marcus, N. W. Gale, M. E. Morrison, C. A. Mason, and G. D. Yancopoulos. Eph family receptors and their ligands distribute in opposing gradients in the developing mouse retina. *Dev. Biol.*, 180(2):786–789, Dec. 1996.
- [47] T. McLaughlin and D. D. M. O’Leary. Molecular gradients and development of retinotopic maps. *Annu. Rev. Neurosci.*, 28:327–355, 2005.
- [48] T. McLaughlin, C. L. Torborg, M. B. Feller, and D. D. M. O’Leary. Retinotopic map refinement requires spontaneous retinal waves during a brief critical period of development. *Neuron*, 40(6):1147–1160, Dec. 2003.

- [49] T. D. Mrsic-Flogel, S. B. Hofer, C. Creutzfeldt, I. Cloëz-Tayarani, J.-P. Changeux, T. Bonhoeffer, and M. Hübener. Altered map of visual space in the superior colliculus of mice lacking early retinal waves. *J. Neurosci.*, 25(29):6921–6928, July 2005.
- [50] X. Nicol, S. Voyatzis, A. Muzerelle, N. Narboux-Nême, T. C. Südhof, R. Miles, and P. Gaspar. cAMP oscillations and retinal activity are permissive for ephrin signaling during the establishment of the retinotopic map. *Nat. Neurosci.*, 10(3):340–347, Mar. 2007.
- [51] M. T. Owens, D. A. Feldheim, M. P. Stryker, and J. W. Triplett. Stochastic interaction between neural activity and molecular cues in the formation of topographic maps. *Neuron*, 87(6):1261–1273, Sept. 2015.
- [52] H. n. Park, Y. Qazi, C. Tan, S. B. Jabbar, Y. Cao, G. Schmid, and M. T. Pardue. Assessment of axial length measurements in mouse eyes. *Optom. Vis. Sci.*, 89(3):296–303, Mar. 2012.
- [53] G. Paxinos. *The Rat Nervous System*. Academic Press, July 2014.
- [54] T. J. Petros, A. Rebsam, and C. A. Mason. Retinal axon growth at the optic chiasm: to cross or not to cross. *Annu. Rev. Neurosci.*, 31:295–315, 2008.
- [55] P. Phongphanphanee, R. A. Marino, K. Kaneda, Y. Yanagawa, D. P. Munoz, and T. Isa. Distinct local circuit properties of the superficial and intermediate layers of the rodent superior colliculus. *Eur. J. Neurosci.*, 40(2):2329–2343, July 2014.
- [56] D. T. Plas, J. E. Lopez, and M. C. Crair. Pretarget sorting of retinocollicular axons in the mouse. *J. Comp. Neurol.*, 491(4):305–319, Oct. 2005.
- [57] S. M. Potter. Distributed processing in cultured neuronal networks. *Prog. Brain Res.*, 130: 49–62, 2001.
- [58] T. Rashid, A. L. Upton, A. Blentic, T. Ciossek, B. Knöll, I. D. Thompson, and U. Drescher. Opposing gradients of ephrin-as and EphA7 in the superior colliculus are essential for topographic mapping in the mammalian visual system. *Neuron*, 47(1):57–69, July 2005.
- [59] M. Reber, P. Burrola, and G. Lemke. A relative signalling model for the formation of a topographic neural map. *Nature*, 431(7010):847–853, Oct. 2004.
- [60] J. R. Sanes and R. H. Masland. The types of retinal ganglion cells: current status and implications for neuronal classification. *Annu. Rev. Neurosci.*, 38:221–246, July 2015.
- [61] T. A. Seabrook, T. J. Burbridge, M. C. Crair, and A. D. Huberman. Architecture, function, and assembly of the mouse visual system. *Annu. Rev. Neurosci.*, 40:499–538, July 2017.

- [62] N. Sherazee and V. A. Alvarez. DiOlistics: delivery of fluorescent dyes into cells. *Methods Mol. Biol.*, 940:391–400, 2013.
- [63] C. S. Sherrington. Observations on the scratch-reflex in the spinal dog. *J. Physiol.*, 34(1-2):1–50, Mar. 1906.
- [64] R. W. Sperry. Chemoaffinity in the orderly growth of nerve fiber patterns and connections. *Proc. Natl. Acad. Sci. U. S. A.*, 50:703–710, Oct. 1963.
- [65] L. Squire, D. Berg, F. E. Bloom, S. du Lac, A. Ghosh, and N. C. Spitzer. *Fundamental Neuroscience*. Academic Press, Dec. 2012.
- [66] B. K. Stafford, A. Sher, A. M. Litke, and D. A. Feldheim. Spatial-temporal patterns of retinal waves underlying activity-dependent refinement of retinofugal projections. *Neuron*, 64(2):200–212, Oct. 2009.
- [67] N. V. Swindale. The development of topography in the visual cortex: a review of models. *Network: Computation in Neural Systems*, 7(2):161–247, Jan. 1996.
- [68] J. W. Triplett, M. T. , J. Yamada, G. Lemke, J. Cang, M. P. Stryker, and D. A. Feldheim. Retinal input instructs alignment of visual topographic maps. *Cell*, 139(1):175–185, Oct. 2009.
- [69] J. W. Triplett, C. Pfeiffenberger, J. Yamada, B. K. Stafford, N. T. Sweeney, A. M. Litke, A. Sher, A. A. Koulakov, and D. A. Feldheim. Competition is a driving force in topographic mapping. *Proc. Natl. Acad. Sci. U. S. A.*, 108(47):19060–19065, Nov. 2011.
- [70] J. W. Triplett, C. Pfeiffenberger, J. Yamada, B. K. Stafford, N. T. Sweeney, A. M. Litke, A. Sher, A. A. Koulakov, and D. A. Feldheim. Competition is a driving force in topographic mapping. *Proceedings of the National Academy of Sciences*, 108(47):19060–19065, 2011.
- [71] D. Tsigankov and A. A. Koulakov. Sperry versus hebb: topographic mapping in Isl2/EphA3 mutant mice. *BMC Neurosci.*, 11:155, Dec. 2010.
- [72] D. N. Tsigankov and A. A. Koulakov. A unifying model for activity-dependent and activity-independent mechanisms predicts complete structure of topographic maps in ephrin-a deficient mice. *J. Comput. Neurosci.*, 21(1):101–114, Aug. 2006.
- [73] F. Valverde. The neuropil in superficial layers of the superior colliculus of the mouse. a correlated golgi and electron microscopic study. *Z. Anat. Entwicklungsgesch.*, 142(2):117–147, Oct. 1973.
- [74] D. J. Willshaw, D. C. Sterratt, and A. Terakiidis. Analysis of local and global topographic order in mouse retinocollicular maps. *J. Neurosci.*, 34(5):1791–1805, Jan. 2014.

- [75] P. A. Yates, A. L. Roskies, T. McLaughlin, and D. D. O’Leary. Topographic-specific axon branching controlled by ephrin-as is the critical event in retinotectal map development. *J. Neurosci.*, 21(21):8548–8563, Nov. 2001.